Energy Research and Development Division

FINAL PROJECT REPORT

Solar-Reflective "Cool" Walls: Benefits, Technologies, and Implementation

Appendix E: Urban Climate Impacts of Cool Walls (Task 3.2 Report)

California Energy Commission
Gavin Newsom, Governor

April 2019 | CEC-500-2019-040-APE

Appendix E:
Urban climate impacts of cool walls (Task 3.2 report)

Jiachen Zhang[1], Arash Mohegh[1], Yun Li[1], Ronnen Levinson[2], George Ban-Weiss[1]

[1] Department of Civil and Environmental Engineering, University of Southern California

[2] Heat Island Group, Lawrence Berkeley National Laboratory

31 May 2018

Abstract

This study for the first time assesses the influence of employing solar reflective "cool" walls on the urban energy budget and summertime climate of the Los Angeles basin. We systematically compare the effects of cool walls to cool roofs, a heat mitigation strategy that has been widely studied and employed, using a consistent modeling framework (Weather Research and Forecasting model). Adoption of cool walls leads to increases in urban grid cell albedo that peak in the early morning and late afternoon, when the ratio of solar radiation onto vertical walls versus horizontal surfaces is at a maximum. In Los Angeles County, daily cumulative increase in grid cell reflected solar radiation from increasing whole-wall albedo (albedo of the entire wall, including its openings) by 0.80 is 783 kJ m^{-2}, 43% of that for increasing whole-roof albedo. Cool walls reduce canyon air temperatures in Los Angeles by 0.43 K (daily average), with the peak reduction (0.64 K) occurring at 09:00 LST and a secondary peak (0.53 K) at 18:00 LST. Per 0.10 whole-wall (whole-roof) albedo increase, cool walls (roofs) can reduce summertime daily average canyon air temperature by 0.048–0.054 K (0.058–0.060 K), yielding a cool-wall to cool-roof temperature reduction ratio of 83 – 90 percent.

If the albedos of windows and doors are unchanged in a cool-wall campaign, these cool-wall air temperature reductions and solar upflux increases should be multiplied by 0.83, the ratio of net wall area (gross wall area minus opening area) to gross wall area in the City of Los Angeles. In the City of Los Angeles, the whole-wall albedo increase from a cool-wall campaign that excludes windows and doors is essentially equal to the whole-roof albedo increase from a cool-roof campaign that modifies the entire roof.

Results reported here can be used to inform policies on urban heat island mitigation or climate change adaptation.

1 Introduction

The urban heat island effect (UHIE) is a phenomenon in which urban areas are warmer than surrounding rural areas, a result of urban-rural differences in land cover and population density. The UHIE can exacerbate challenges associated with high temperatures in urban areas including (a) human health impacts from extreme heat (Palecki et al., 2001), such as heat stroke, heat exhaustion rates, and premature deaths; and (b) daily total and peak air conditioning energy use during summer (Kolokotroni et al., 2006). Several important environmental processes, which are driven by the effects of urban land expansion on surface-atmosphere coupling, can aggravate or mitigate the UHIE. First, widespread application of materials with high solar absorptance (e.g., asphalt concrete and many roofing materials) in urban areas increases absorption of sunlight. Second, extensive use of materials with high heat capacity increases retention of sunlight throughout the day. Third, the geometry of urban canyons (i.e., the space between buildings and above streets) can trap both shortwave (solar) and longwave (thermal infrared) radiation (Theeuwes et al., 2014). Fourth, lack of vegetation cover in cities reduces evaporative cooling and shading of the ground surface, thereby increasing urban temperatures (Taha, 1997). Fifth, increases in soil moisture from irrigation in urban areas can increase evaporative fluxes and cool cities during the day, while at night causing increases in upward ground heat fluxes (due to the increase in soil moisture and thermal conductivity) and therefore nocturnal warming (Vahmani et al., 2016). Sixth, changes in surface roughness from urbanization can also alter wind flows and vertical mixing (Vahmani et al., 2016), with subsequent effects on temperatures that can vary by location. Finally, human activities and industrial processes contribute to releasing waste heat in cities (Fan and Sailor, 2005; Oke et al., 1991) .

To lessen the UHIE, heat mitigation strategies have been proposed and employed in some locations to alter the energy balance in cities and decrease temperatures. For example, planting trees and/or adopting vegetative roofs could increase evaporative cooling and reduce urban temperatures (Li et al., 2014). Increasing the albedo, or solar reflectance (ratio of reflected to incident sunlight) of roofs, walls, and pavements could reduce solar heat gain, lower surface temperatures, decrease heat transfer from the surface to the atmosphere, and consequently cool the outside air. Heat mitigation strategies can also influence urban climate by changing the hydrological cycle (Georgescu et al., 2014).

The effects of solar-reflective “cool” roofs on urban climate have been well studied in previous research. Large-scale implementation of cool roofs has been predicted to effectively reduce city-wide air temperatures in Athens, Greece (Synnefa et al., 2008); Sacramento (Taha, 2008); and Baltimore-Washington (Li et al., 2014). In Los Angeles, the reduction of peak air temperature induced by increasing both roof and pavement albedo was estimated to reach 1.5 K (Rosenfeld et al., 1998), while a newer study (Millstein and Menon, 2011) estimated the reduction at 13:00 local standard time (LST) in summer to be 0.5 K. In addition, Vahmani et al. (2016) concluded that widespread adoption of cool roofs could reduce Southern California summer urban air

temperatures by 0.9 K at 14:00 LST and by 0.5 K at 22:00 LST. Santamouris (2014) summarized previous literature and concluded that daily average ambient temperatures are expected to decrease linearly with average grid cell albedo increase in cities, declining 0.3 K per 0.1 albedo increase. (We note here that grid cell albedo represents a "bird's eye view" of both impervious and pervious surfaces within modeled urban regions.)

Cool pavements have been studied less than cool roofs. While they are both horizontal surfaces, temperature reductions per unit facet albedo increase can differ between them in part because cool pavements are at the bottom of the urban canyon while roofs are at the top. Mohegh et al. (2017) simulated the influence of employing cool pavements on near-surface air temperatures in Californian cities. They found that increasing pavement albedo by 0.40 could lead to annual average air temperature reductions at 14:00 LST ranging by city from 0.19 K to 0.87 K. Temperatures at 14:00 LST declined by 0.32 K per 0.10 increase in grid cell average albedo.

Despite previous studies that have examined the effects of raising albedo of horizontal surfaces in different cities, the influence of increasing the albedo of vertical surfaces (e.g., walls) on temperatures has not yet been systematically investigated. The climate effects of increasing wall albedo are expected to differ from those for cool roofs. First, increasing wall albedo and roof albedo by the same amount will influence the energy budget of the urban canopy (i.e., the urban canyon plus roof surfaces) differently for four reasons:

(a) Diurnal cycles of solar irradiance (incident radiative power per unit area) and daily solar irradiation (incident radiative energy per unit area) received by vertical walls differ from those received by (nearly) horizontal roofs. For example, in July, the north, east, south and west walls of a building in San Diego and Fullerton, CA collectively typically receive about 40% as much daily solar irradiation as its roof (See Tables A1 and A2 in Task Report Appendix A). Figure 1 in the supplemental information compares the diurnal cycle of irradiance on roofs and walls.

(b) Walls make up a different fraction of urban areas than do roofs (see Section 2.3 for more details).

(c) Walls can be shaded when sun is low, so the fraction of wall area that is illuminated varies by time. In our study, we assume that roofs are not shaded. (In the real-world, non-uniform building heights and trees can lead to roof shading, but we ignore these effects in this study.)

(d) A portion of the solar radiation that is reflected by walls is absorbed by opposing walls and pavements, and is thus trapped in the canyon. Solar radiation reflected by roofs, on the other hand, mostly escapes the canopy without being absorbed by other urban facets. Unlike cool roofs, the effect of cool walls depends of the height to width ratio of the urban canopy.

Hence, solar reflections from cool walls differ in timing and magnitude from those from cool roofs.

Second, atmospheric temperature changes induced by cool surfaces are determined not only by the change in the canyon energy budget but also by the diurnal cycle in surface-atmosphere interactions. Diurnal variations in wind speeds, planetary boundary layer (PBL) heights, and atmospheric stability can influence the relationship between changes in the surface energy budget and resulting atmospheric temperature reductions (Bonan, 2010). Cool walls and roofs induce different diurnal cycles in reflected solar radiation. Thus, the diurnal cycles in surface-atmosphere coupling contribute to differences in air temperature change. In other words, even if increases in daily reflected solar radiation were the same for cool walls and roofs, their different diurnal cycles would be expected to lead to different daily average air temperatures.

Lastly, walls are in the urban canyon whereas roofs are at the top of the canopy. This means that walls may more directly influence in-canyon air temperatures than roofs, while roofs may more directly influence above-canopy air temperatures.

In this study, we use a regional climate model, coupled to an urban canopy model, to investigate how adopting cool walls would influence albedo, reflection of sunlight, and near-surface air temperature in the Los Angeles basin. We adopt a new parameterization that diagnoses near-surface air temperature within the urban canyon, which in turn affects pedestrian thermal comfort and building energy use. A suite of additional cool roof simulations systematically compares the climate effects of cool walls to those of cool roofs within a consistent modeling framework.

2 Methodology

2.1 Model description

We use the Weather Research and Forecasting model (WRF) version 3.7 (Skamarock et al., 2008)to investigate the effects of raising wall albedo on near-surface canyon air temperatures in the Los Angeles basin. WRF is developed collaboratively by the National Center for Atmospheric Research (NCAR), the National Oceanic and Atmospheric Administration (NOAA) and other institutes, and is widely used to study regional-scale meteorology and climate.

WRF provides several parameterizations that can be used to represent processes that occur at resolutions finer than model grid cells. We summarize here the parameterizations chosen for our simulations. Physics schemes include the Rapid Radiative Transfer Model (RRTM) scheme for long-wave radiation (Mlawer et al., 1997), the Goddard shortwave scheme (Chou and Suarez, 1994) for shortwave radiation, the Yonsei University scheme (Hong et al., 2006) for the planetary boundary layer, and Lin et al. scheme for cloud microphysics (Lin et al., 1983). To simulate cumulus clouds in the middle and outer domains, the Kain-Fritsch convective parameterization is used (Kain, 2004). The Noah Land Surface Model (Chen and Dudhia, 2001)

couples the land surface and atmosphere to compute exchanges in energy (e.g., latent and sensible heat fluxes), momentum, and water. A single-layer urban canopy model (UCM) simulates the influence of urban surface-atmosphere coupling (Chen et al., 2011).. Parameterizations for physics are chosen to be consistent with our previous modeling studies for Southern California (Vahmani and Ban-Weiss, 2016a, 2016b), which were extensively evaluated by comparing to observations.

The National Land Cover Database for 2006 is used for land cover type classification in the model (Fry et al., 2011). For urban grid cells (i.e., cells dominated by urban land cover), we use impervious surface data from the National Land Cover Database (NLCD) (Wickham et al., 2013) to compute grid cell specific impervious fractions (i.e., the fraction of each grid cell covered by impervious surfaces). The urban canopy model resolves surface-atmosphere exchange for the impervious part of the grid cell, while the Noah model is used for the pervious portion of urban grid cells. Note that the Noah Land Surface model also handles non-urban grid cells. Urban land use classification and urban morphology will be discussed in Section 2.3.

Following (Vahmani and Ban-Weiss, 2016b), we have improved the default version of the WRF model by utilizing MODIS satellite observations to determine grid cell specific green vegetation fraction and leaf area index for pervious areas (i.e., for both the pervious portion of urban grid cells and for non-urban cells). Previous research has found that accounting for high resolution heterogeneity in land surface properties in urban areas can improve model simulations when comparing to observations of meteorology in Los Angeles (Vahmani et al., 2016).

2.2 Shortwave radiation calculations in the urban canopy model

In the single-layer urban canopy model (UCM) employed in WRF (Kusaka et al., 2001), the urban canopy is represented as an infinitely long street (a.k.a. ground, or canyon floor) bounded by two infinitely long buildings of identical width. That is, there is no separation between adjacent buildings on the same side of the street. Recall that we refer to the urban canopy as the canyon plus roof surfaces.

Direct (beam) and diffuse solar radiation are tracked separately in our model. At solar noon, most beam sunlight strikes horizontal surfaces (roofs and ground), rather than vertical surfaces (walls). In early morning and late afternoon, the ratio of beam vertical radiation to beam horizontal radiation is higher than that at solar noon. Buildings shade the ground when the sun is not at zenith, reducing the ground's solar irradiance and solar heat gain. Since in the canopy model all sunlight not incident on roofs strikes walls or the ground, the beam solar radiation (power) intercepted by the sun-facing wall equals beam horizontal irradiance (power/area) times the length of the ground shadow. Canyon orientation (i.e., the angle between canyon centerline and north) and solar position are considered in the calculations of ground shadow length throughout the day. Eight canyon orientations (0˚, 45˚, 90˚, 135˚, 180˚, 225˚, 270˚, 315˚) are considered, and the shadow length is averaged among the results. Ground shadows are longest

when the sun is low and shortest when the sun is high. Thus, the fraction of global horizontal irradiance that is incident on the ground peaks at solar noon, while that incident on walls reaches its minimum at solar noon and maximum at peaks in the early morning and late afternoon (Figure 2 in Task Report Appendix A).

The diffuse part of solar radiation can strike all impervious facets (roofs, walls, and ground). Downwelling diffuse solar irradiances on wall and ground surfaces are proportional to the view factors from wall to sky and from ground to sky, respectively. Each facet is assumed to reflect sunlight diffusely. The view factors from ground to wall, from wall to ground, and from sun-facing wall to sun-opposing wall influence the reception of reflected radiation by walls and ground. Note that radiation reflected twice by facets is assumed to fully escape from urban canopy. For example, absorption within the canopy of light reflected from wall to wall to ground is ignored in the model.

Note that even though WRF-UCM includes a “shadow model” that treats direct and diffuse radiation separately, as aforementioned, the default code of WRF-UCM has the “shadow model” turned off. Thus, all solar radiation is treated as diffuse and shadows casted by buildings is not considered. (See Line 853 of module_sf_urban.F in WRF3.7 where SHADOW = .false.) We turn on the shadow calculations by setting SHADOW = .true. We also add to the default shadow model wall-to-wall reflection effects following Kusaka et al. (2001).

Downward solar radiation that is not absorbed by roofs, walls, and ground is reflected out of the canopy as upwelling solar radiation. UCM calculates canopy albedo as the ratio of upwelling sunlight to downwelling sunlight at the horizontal plane bounding the top of the canopy. The changes to canopy albedo upon increasing wall albedo are computed here using the single-layer urban canopy model. Canopy albedo represents the aggregated “above-canopy” albedo of all facets in the urban portion of grid cells, not including contributions from the non-urban portion of the grid cell. Since only the urban portion of the grid cell is modified, changes in grid cell albedo are then computed as change in canopy albedo multiplied by urban fraction (Figure 1c). Note that canopy and grid cell albedo are diagnostic variables and are not used in other model calculations.

2.3 Urban land use type classification and corresponding canopy morphology

Urban morphology in the UCM is described by roof width (R), building height (H), and ground width (W). The UCM uses the urban morphology to compute (a) solar irradiance (power/area) incident onto each facet; (b) shortwave radiation (power/area) reflection and longwave radiation (power/area) transfer from each facet to other canyon facets and to the sky; and (c) area weighting factors for averaging solar absorption (power/area) and sensible heat fluxes (power/area) among facets.

Data describing spatially resolved urban morphology from the National Urban Database and Access Portal Tool (NUDAPT) are used where available. NUDAPT data (Ching et al., 2009) cover only a small portion of our domain, but include downtown Los Angeles, where unusually tall buildings are found. For grid cells where NUDAPT data are not available, we derive urban morphology as follows.

The National Land Cover Database (NLCD) for 2006 is used for land cover type classification in the model (Fry et al., 2011). NLCD includes three urban land use types: low-intensity residential, high-intensity residential, and commercial/industrial. In the WRF UCM, we define different urban morphologies for each of the three urban types.

For each urban land use type, urban canopy morphology (i.e., ground width, building height, and roof width in Table 1) is set based on two real-world datasets for Los Angeles County: LARIAC (2014) and LARIAC (2016). LARIAC (2016) provides information for every building in Los Angeles County, including ZIP Code, roof area, building height, and shape. LARIAC (2014) provides the geographical centerlines for each street in Los Angeles County. Urban morphologies in the UCM are derived satisfying (a) H/W in the UCM as the ratio between building height from LARIAC (2016) and ground width from LARIAC (2014), and (b) $2 \times H/R$ in the UCM as the ratio of gross wall area to roof area in LARIAC (2016).

Every building within each ZIP Code in Los Angeles County is classified as "low-intensity residential," "high-intensity residential," or "commercial/industrial," based on the dominant NLCD land use type (LUT) in that ZIP Code. Each building class is assigned a single representative building height H in the 2D UCM, computed as the mean building height in LARIAC (2016) for buildings in that class. Each building class is also assigned a single representative roof width R in the 2D UCM, set to match $2\,H/R$ to the median ratio of whole-building gross wall area to roof area in LARIAC (2016) for buildings in that class. Each building's roof area is set to its LARIAC (2016) footprint area, and its whole-building gross wall area is calculated as its LARIAC (2016) building height multiplied by its LARIAC (2016) building perimeter. The median ratio of gross wall area to roof area by building class is 1.95 for low-intensity residential, 1.96 for high-intensity residential, and 2.10 for commercial/industrial. Weighted by impervious area within each land use type (derived from NLCD), the mean value of these median ratios is 1.97.

Ground width W was computed by combining the building and street centerline datasets. For each road segment, we computed the distance between the street centerline in (LARIAC, 2014) and the nearest building (LARIAC, 2016). We doubled this distance to estimate ground width, then averaged ground width by ZIP Code. Finally, with knowledge of the dominant NLCD type per ZIP-Code, W was computed by taking the average of ZIP-Code level values of ground width per NLCD type.

Table 1. Two-dimensional urban morphology used in our urban canopy model (UCM), derived from LARIAC (2014) and LARIAC (2016) descriptions of the three-dimensional morphology of Los Angeles County.

Urban land use type	Building height H (m)	Roof width R (m)	Ground width W (m)
Low-intensity residential	5.8	6.0	26.6
High-intensity residential	5.3	5.4	24.3
Commercial/industrial	6.5	6.2	27.1

2.4 Canyon air temperature

For urban grid cells (i.e., grid cells dominated by urban land cover; Figure 1b), the standard WRF diagnoses and outputs canyon temperature and 2-m grid cell air temperature. Canyon temperature is effectively an aggregated skin temperature for walls and ground. This temperature is used in calculations of sensible heat flux from the canyon to the atmosphere. The calculation for the default grid cell 2-m air temperature diagnosed by WRF uses the roughness length of grass, leading to unphysical results in urban grid cells (Li and Bou-Zeid, 2014).

To better simulate the temperature near the ground level in cities, we implement the parameterization proposed by Theeuwes et al. (2014) to calculate near-surface air temperature within the urban canyon, which we refer to as canyon air temperature.

The canyon air temperature is parameterized as

$$T_{\mathrm{c}} = \frac{H_{\mathrm{c}}\, r_{2\mathrm{m}}}{\rho\, C_{\mathrm{p}}} + T_{\mathrm{a}} \tag{1}$$

where H_{c} is the total sensible heat flux (power/area) from canyon surfaces (i.e., walls and ground) to the lowest layer of the atmospheric model, C_{p} (J kg^{-1} K^{-1}) is the specific heat capacity of dry air, ρ (kg m^{-3}) is the density of air, and T_{a} (K) is the air temperature in the lowest layer of atmospheric model.

Stability correction is used to account for the influence of atmospheric stability on heat transfer based on Monin-Obukhov similarity theory. $r_{2\mathrm{m}}$ is transfer resistance that is applied between the lowest layer of the atmosphere model and two meters above ground (Theeuwes et al., 2014), computed as

$$r_{2\mathrm{m}} = \frac{1}{\kappa u_*}\left\{\ln\left(\frac{z_{\mathrm{a}}}{z_{2\mathrm{m}}}\right) - \Psi\left(\frac{z_{\mathrm{a}}}{L}\right) + \Psi\left(\frac{z_{2\mathrm{m}}}{L}\right)\right\} \tag{2}$$

where κ is the dimensionless von Kármán mixing-length constant (i.e., 0.4), u_* (m s^{-1}) is friction velocity, L (m) is the Obukhov length (i.e., the height at which turbulence kinetic energy generated by wind shear is equal to that generated by buoyancy), z_{2m} (m) is the height of 2 m, and z_a (m) is the height of the lowest atmospheric model layer (Theeuwes et al., 2014).

Ψ (unitless) is the stability correction function, which is parameterized as

$$\Psi\left(\frac{z}{L}\right) = \begin{cases} 2\ln\left\{\frac{1+(1-16\frac{z}{L})^{\frac{1}{2}}}{2}\right\} & (\frac{z}{L} < 0) \\ -5\frac{z}{L} & (\frac{z}{L} \geq 0) \end{cases} \quad (3)$$

where z is height (m).

In this study, we report changes in canyon air temperature because it is more applicable to human thermal comfort than the grid cell near-surface air temperature.

2.5 Simulation domain

Three nested domains are simulated at resolutions of 18 km, 6 km, and 2 km, respectively (Figure 1a). The outermost domain (d01) covers California; the middle domain (d02) simulates southern California; and the innermost domain (d03) encompasses the Los Angeles basin and San Diego. The domain is the same as that used in our previous modeling work (Vahmani et al., 2016; Vahmani and Ban-Weiss, 2016a; Vahmani and Ban-Weiss, 2016b). Each inner domain uses values from the adjacent outer domain as boundary conditions. The outermost domain (d1 in Figure 1a) uses the North American Regional Reanalysis (NARR) dataset (Mesinger et al., 2006) as boundary conditions. The NARR dataset has a spatial resolution of 32 km and temporal resolution of 3 hours. The atmosphere is simulated using 30 layers in the vertical. Urban areas in Los Angeles County are included in our analysis on diurnal cycles.

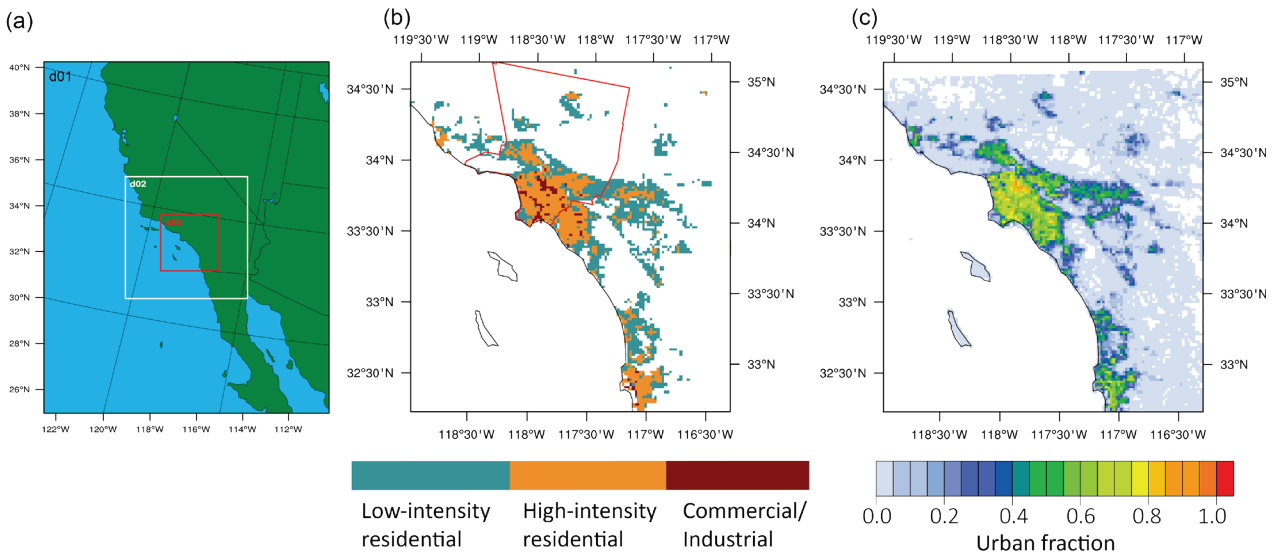

Figure 1. (a) Nested simulation domains d01 (Western United States), d02 (Central and Southern California), and d03 (Southern California). (b) Dominant urban land use types in domain d03; red outline bounds urban areas in Los Angeles County considered in our analysis of diurnal air temperatures cycles. (c) Urban fractions in domain d03.

2.6 Simulation design

Our analysis of the influence of cool walls on the climate of Southern California considers three scenarios: CONTROL, in which ground, whole-roof, and whole-wall albedos are each set to 0.10; COOL_WALL_LOW, in which whole-wall albedo is raised to 0.50; and COOL_WALL_HIGH, in which whole-wall albedo is raised to 0.90. Here whole-roof albedo is the ratio of sunlight reflected from the entire roof to that incident on the entire roof, including openings (e.g., skylights) and roof-mounted equipment, while whole-wall albedo is the ratio of sunlight reflected from the entire wall to that incident on the entire wall, including openings (windows and doors). To compare the effect of increasing whole-wall albedo to that of raising whole-roof albedo, we add two more scenarios: COOL_ROOF_LOW, in which whole-roof albedo is raised to 0.50; and COOL_ROOF_HIGH, in which whole-roof albedo is raised to 0.90 (Table 2). In this way, the whole-facet albedo increases are 0.40 for COOL_WALL_LOW and COOL_ROOF_LOW scenarios, and 0.80 for COOL_WALL_HIGH and COOL_ROOF_HIGH scenarios. The albedo values are chosen to gauge the upper bound effect of applying cool walls and roof, and to test the linearly of canyon air temperatures with increasing wall and roof albedos. Note that cool surface albedos in cases COOL_WALL_HIGH (wall albedo 0.90) and COOL_ROOF_HIGH (roof albedo 0.90) are higher than those of actual cool walls and roofs, especially after weathering and soiling. For example, the albedo of an initially bright-white roof might fall to about 0.60 - 0.70 from about 0.80 - 0.90 after several years of exposure (Sleiman et al. 2011; Berdahl et al. 2008). The initial albedo of a non-white cool surface, such as a "cool colored" roof, typically ranges from about 0.25 to about 0.50 (Levinson et al. 2007), and its albedo loss upon exposure tends to be smaller than that experienced by a bright-white roof (Sleiman et al. 2011). Note that

percentage of sunlight reflected by walls that escapes the urban canopy (Table 2) is calculated from urban morphology and wall albedo in Task Report Appendix B.

We perform three ensemble simulations per scenario to reduce the influence of model internal variability on results. The ensemble simulations are carried out by initiating the model simulations at different times (14:00 LST on 28 June 2012, 14:00 LST on 29 June 2012, and 14:00 LST on 30 June 2012). Ensemble means are reported for each scenario.

Simulations are performed for about 14 days (28 June 2012 to 11 July 2012). Due to intrinsic uncertainties in initial conditions, modeled results at the start of the simulations are unreliable (Warner, 2011). A previous study with the same model configuration discarded the first 12 simulated hours as model "spin-up" (Vahmani et al., 2016). In this study, the first three to five days are discarded as "spin-up," and only the results from 3 July 2012 to 11 July 2012 are used in our analysis of changes in canyon air temperatures and albedo.

Table 2. Wall and roof albedos in five scenarios. Ground albedo is 0.10 in each scenario.

Scenario	Wall albedo	Roof albedo	Fraction of sunlight reflected by walls that escapes urban canopy (%)
CONTROL	0.10	0.10	50
COOL_WALL_LOW	0.50	0.10	54
COOL_WALL_HIGH	0.90	0.10	59
COOL_ROOF_LOW	0.10	0.50	50
COOL_ROOF_HIGH	0.10	0.90	50

2.7 Caveats

The results later presented in this report rely on the ability of the model to accurately simulate atmospheric processes and surface-atmosphere interactions. Results may vary depending on the modeling systems employed. The climate effects of cool walls and roofs are expected to vary depending on urban morphology and impervious fraction, as well as the baseline climate of the city under investigation (Millstein and Menon, 2011; Mohegh et al., 2017).

We focus our analysis on Los Angeles County, and accordingly set the urban canopy morphology and impervious fraction based on region-specific GIS datasets.

If a cool-wall campaign does not change the albedos of doors and windows, all cool-wall air temperature reductions and solar upflux increases reported in this study should be multiplied by the ratio of net wall area (gross wall area minus area of openings) to gross wall area. We propose a ratio of 0.83, which is that computed for the City of Los Angeles (Appendix A, Table A4).

3 Results and discussion

3.1 Diurnal cycle of grid cell albedo and reflected solar radiation

Figure 2a shows the diurnal cycle of albedo changes induced by cool walls averaged over urban grid cells in Los Angeles County. Figure 2a shows that during the daytime, the urban grid cell albedo rise induced by increasing whole-wall albedo to 0.90 from 0.10 (COOL_WALL_HIGH – CONTROL) is smallest (0.02) at solar noon, and greatest (~0.10) in the early morning (06:00 LST) and late afternoon (18:00 LST) in Los Angeles County. (The average sunrise and sunset times for our analysis period are 04:48 LST and 19:07 LST, respectively.) This diurnal cycle occurs because wall albedo has its maximum influence on grid cell albedo in the early morning and late afternoon as the ratio of solar irradiance on vertical surfaces versus horizontal surfaces reaches its maximum (Figures A1 and A2 in Task Report Appendix A). On the other hand, increasing whole-roof albedo by 0.80 (COOL_ROOF_HIGH – CONTROL) will result in a constant urban grid cell albedo rise of 0.07 because the modeled roof is horizontal. Increasing whole-roof albedo, as compared to increasing whole-wall albedo by the same amount, can lead to a greater increase in average urban grid cell albedo in Los Angeles County from 07:00 to 17:00 LST.

Figure 2b shows the diurnal cycle of changes in grid cell upflux (upwelling sunlight) reflected through the horizontal plane bounding the urban canopy. The upflux is calculated as the product of downflux (global horizontal irradiance, or GHI) and grid cell albedo. GHI peaks at noon (Figure 2c). The increase in upflux induced by cool walls reaches its two greatest values at 10:00 and 15:00 LST, a result of diurnal variations of both GHI and grid cell albedo increase. Therefore, cool walls can reject more sunlight from the urban canopy in the late morning and early afternoon than in other daylight hours. The diurnal cycles of increases in reflected radiation induced by cool roofs are concave up with larger diurnal variations than for cool walls, following the trend of horizontal irradiance (Figure 2c). The increase in solar reflection reaches the maximum at solar noon, the time associated with peak horizontal irradiance.

Relative to CONTROL, the daily increase in grid cell upflux for COOL_WALL_HIGH (783 kJ m^{-2}) is 43% of that for COOL_ROOF_HIGH (1841 kJ m^{-2}) (Table 3). Three factors contribute to the difference in increased reflected solar radiation induced from cool walls versus roofs: (a) gross wall area is a factor of ~2 larger than roof area in Los Angeles County; (b) solar irradiance (W m^{-2}) onto walls and roofs differ, and daily cumulative solar irradiation (J m^{-2}) onto walls (2,857 J m^{-2}) is 38% of that onto roofs (7,575 J m^{-2}) over the analysis period (Figure A1 in Task Report Appendix A); and (c) in our model the solar radiation reflected by walls is partially (50-59%) absorbed by walls and pavements, while all solar radiation reflected by roofs escapes the canopy (Table 2).

In our simulations, the increase in whole-wall albedo for COOL_WALL_HIGH – CONTROL (0.80) is twice that for COOL_WALL_LOW – CONTROL (0.40) (Table 2). These whole-wall albedo increases lead to grid cell albedo increases at 06:00 LST and 12:00 LST that differ by a factor of ~2 (Table 3). This means that the urban increases in grid cell albedo are proportional to whole-wall albedo rises. Similarly, increase in daily cumulative reflected solar radiation scale approximately linearly with whole-wall albedo rise. These linear relationships also apply to cool roofs.

Table 3. Urban grid cell albedo, upflux (reflected solar radiation), and canyon air temperature by time of day in urban areas of Los Angeles County (shown in Figure 1b) , reporting absolute values for scenario CONTROL, and changes from CONTROL for the four remaining scenarios. [a]

Scenario	Albedo at 06:00 LST	Albedo at 12:00 LST	Daily solar upflux (kJ m^{-2})	Daily (24-hour) average canyon air temperature (K)	Canyon air temperature (K) at 14:00 LST	Canyon air temperature (K) at 20:00 LST	Daily (24-hour) average canyon air temperature (K) per 0.10 whole-facet albedo increase
CONTROL	0.143	0.148	4,339	295.2	302.0	294.5	295.2
COOL_WALL_LOW minus CONTROL	0.045	0.008	371	-0.19	-0.19	-0.18	-0.048
COOL_WALL_HIGH minus CONTROL	0.097	0.017	783	-0.43	-0.41	-0.40	-0.054
COOL_ROOF_LOW minus CONTROL	0.033	0.033	925	-0.23	-0.34	-0.18	-0.058
COOL_ROOF_HIGH minus CONTROL	0.065	0.065	1,841	-0.48	-0.72	-0.36	-0.060

[a] All values are averages from July 3 to July 12.

3.2 Spatial variation of grid cell albedo and albedo increase

Figure 3 shows spatial variations in grid cell albedo for CONTROL (Figure 3a), as well as albedo changes due to raising wall and roof albedos by 0.80 (Figure 3b,c). Spatial variability in grid cell albedo increase (Figure 3b,c) is caused by spatial variation in urban fraction (Figure 1c) and urban canyon morphologies. Urban grid cells with higher urban fraction (Figure 1c) tend to have larger albedo increases after implementing cool walls or roofs. For example, the whole-wall albedo increases for COOL_WALL_HIGH – CONTROL in downtown Los Angeles can reach as high as 0.24 at 06:00 LST, which is larger than the spatial average over urban grid cells (0.10). Consistent with Figure 2, the grid cell albedo increase from adopting cool walls is larger at 06:00 than 12:00 LST. At 06:00 LST, grid cell albedo increase induced by adopting cool walls is larger than that induced by cool roofs with the same facet albedo rise.

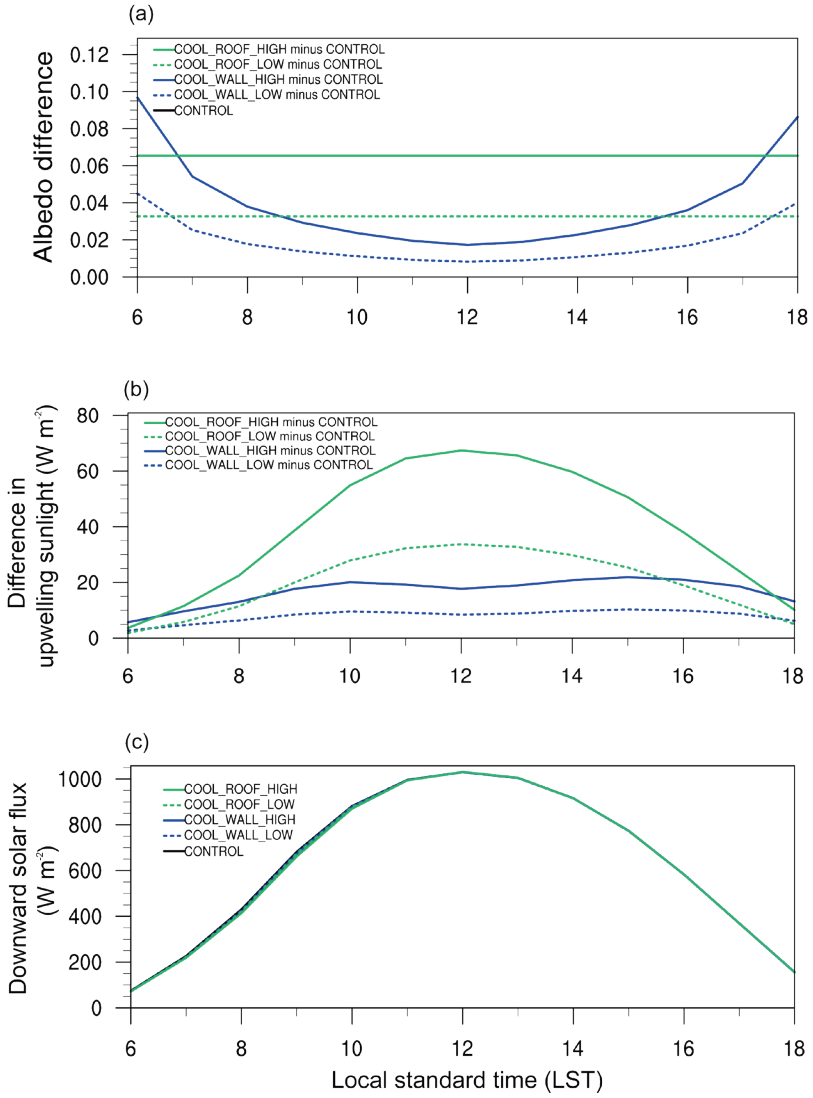

Figure 2. Diurnal cycles of difference from the CONTROL scenario for (a) grid cell albedo and (b) upwelling sunlight for the remaining scenarios COOL_ROOF_HIGH, COOL_ROOF_LOW, COOL_WALL_HIGH, and COOL_WALL_LOW; and (c) diurnal cycle of downward solar radiation (global horizontal irradiance) for the five scenarios. Values represent spatial averages in Los Angeles County (shown in Figure 1b) for urban grid cells from 00:00 LST on July 3 to 00:00 LST on July 12. We show hours of the day when downward solar flux is greater than 5 W m^{-2}.

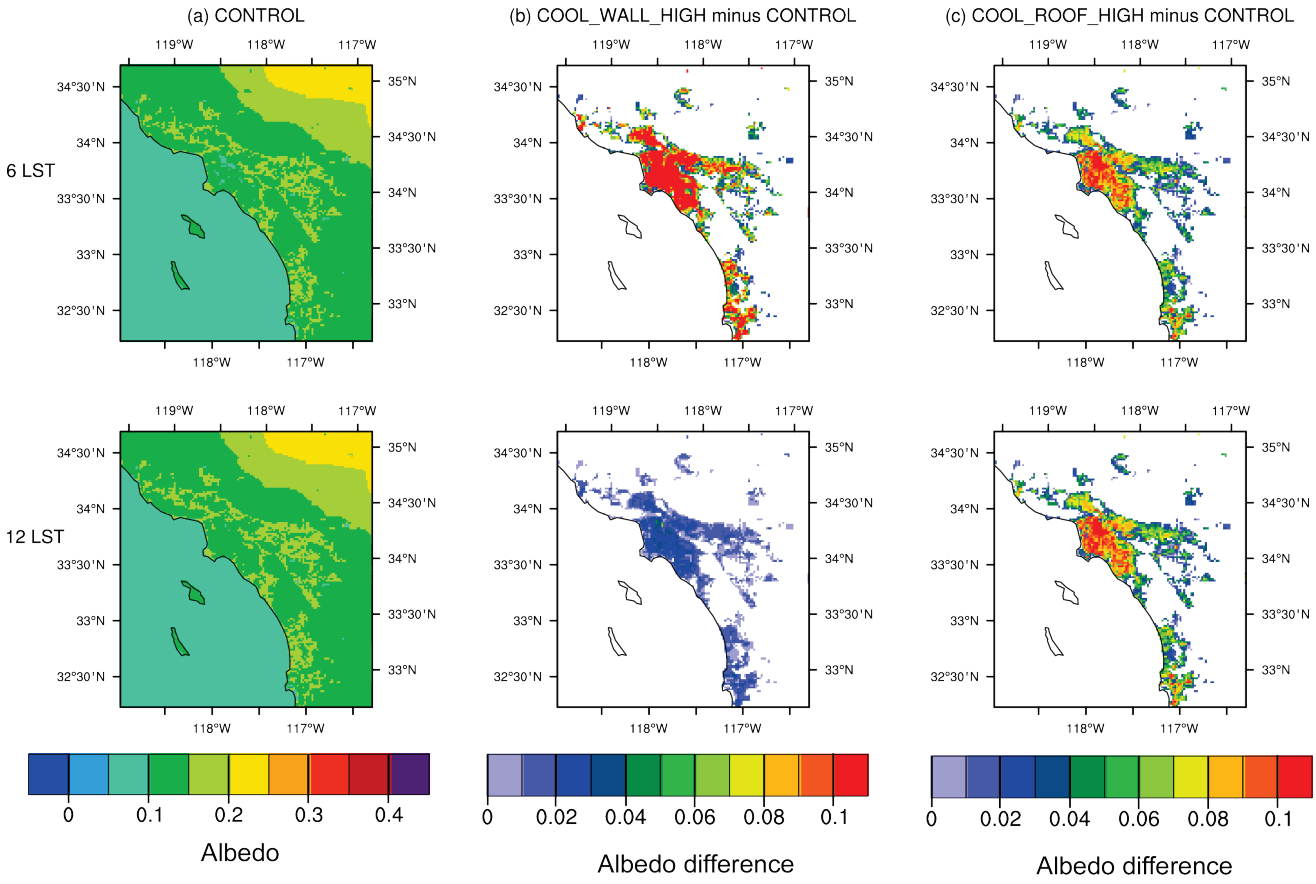

Figure 3. Simulated grid cell albedo at 06:00 LST (top) and 12:00 LST (bottom) for (a) CONTROL, as well as the albedo differences (b) COOL_WALL_HIGH – CONTROL and (c) COOL_ROOF_HIGH – CONTROL. Values are temporally averaged over the period of 00:00 LST on July 3 to 00:00 LST on July 12.

3.3 Diurnal cycle of canyon air temperatures and temperature changes

Figure 4 shows the diurnal cycle of canyon air temperatures for each simulation, and changes in temperatures upon raising whole-wall or whole-roof albedo, spatially averaged over the urban regions of Los Angeles County. Figure 4a shows that in each scenario, canyon air temperature reaches its maximum at 13:00 LST. Peak (greatest) air temperature reduction for cool walls (i.e., 0.65 K for COOL_WALL_HIGH – CONTROL and 0.28 K for COOL_WALL_LOW – CONTROL) occurs at 09:00 LST (Figure 4b). There is a second (smaller) peak in air temperature reduction observed at 18:00 LST. We hypothesize three factors contributing to the shape of the simulated diurnal cycles for canyon air temperature changes due to cool wall adoption. First, increases in reflected solar radiation and reductions in solar heat gain induced by cool walls are greatest at 10:00 and 15:00 LST (Figure 2b). Second, increasing albedo leads to solar heat gain reductions that accumulate throughout the day. Reductions in the surface temperature of thermally massive structures are related to decreases in accumulated, rather than instantaneous, solar

heat gain. Third, the height of the planetary boundary layer (PBL) has a diurnal cycle that is concave down, with a maximum occurring ~13:00 LST (Figure A3 in Task Report Appendix A). Shallower PBL heights reduce the volume of air heated by sensible heat fluxes. This means that a given reduction in sensible heat flux caused by surface temperature decreases would lead to larger reductions in atmospheric heating rate (temperature/time) in the boundary layer when PBL heights are shallow versus deep. Thus, sensible heat flux decreases from cool wall adoption are expected to have larger air temperature effects when the PBL is shallow. [Previous research has highlighted the importance of diurnal cycle in PBL height in determining urban air temperatures; higher PBL heights in urban areas relative to rural areas can contribute to a morning urban cool island (Theeuwes et al., 2015). While this study is not directly related to our research, it shows how PBL height can influence atmospheric heating and air temperature in urban areas.]

Task Report Appendix C considers how PBL height, increase in upflux, and the accumulation of solar heat gain affect diurnal cycles of canyon air temperature reduction from adopting cool walls and cool roofs. All three factors contribute to the greatest reduction in canyon air temperature induced by cool walls at 09:00 LST, which is one hour before wall irradiance peaks and a time at which the PBL height is relatively low.

For cool roofs, the peak temperature reduction of 0.88 K (COOL_ROOF_HIGH – CONTROL) occurs at 10:00 LST. This peak temperature reduction occurs later in the morning than for cool walls because of the difference in diurnal cycle of increased reflected solar radiation (Figure 2a), which reaches its maximum at solar noon for roofs rather than in the morning and afternoon for walls. A previous study on cool pavements (Mohegh et al., 2017) also found that near-surface air temperature reductions peaked in the morning and the evening. They hypothesized that it was due to the combined effects of diurnal cycles in solar irradiance, accumulated solar heat gain, and PBL height.

From 09:00 to 17:00 LST, the canyon air temperature reduction induced by cool roofs is greater than that from cool walls for equal increases in whole-facet albedo (Figure 4b). This can be attributed to the higher increase in reflected solar radiation that escapes the urban canopy from cool roofs versus walls. However, cool walls (relative to cool roofs) create higher canyon air temperature reductions per increase in reflected solar radiation from the canopy at most times of day (Figure A4 in Task Report Appendix A). This is likely because walls are in the urban canyon, so they can more directly cool canyon air than roofs. In addition, for equal increases in whole-facet albedo, cool walls lead to a greater cooling at night relative to cool roofs. The atmosphere is stable at night, meaning that there is little vertical mixing. This means that above-canopy air temperature reductions from cool roofs would undergo less mixing into the canyon, and thus have less effect on canyon air temperatures relative to cool walls at night.

As shown in Table 2, canyon air temperature reductions for COOL_WALL_HIGH relative to CONTROL at 14:00 and 22:00 LST are about the same (0.41 K and 0.40 K, respectively). The reduction at 14:00 LST is lower than that induced by cool roofs (0.72 K), while the cool-wall

reduction at 22:00 LST is higher than that induced by cool roofs (0.36 K) for equal increases in whole-facet albedo.

Increasing whole-wall albedo by 0.40 and 0.80 reduces daily average canyon air temperatures by 0.19 K and 0.43 K, respectively. The daily average canyon air temperature reductions induced by cool walls are slightly less than those induced by cool roofs with the same whole-facet albedo increase (Table 3). On the other hand, for a daily cumulative grid cell upflux increase of 1 J m^{-2}, the daily canyon temperature reduction induced by cool walls would be 0.55 μK, twice that for cool roofs (0.26 μK).

The ratio of the daily average temperature reduction for COOL_WALL_HIGH – CONTROL to that for COOL_WALL_LOW – CONTROL (0.43 K / 0.19 K = 2.3) is close to the ratio of the whole-wall albedo rises for the two scenarios (0.80 / 0.40 = 2) (Table 3), indicating that the average temperature reduction induced by cool walls is approximately proportional to increase in wall albedo. A similar linear relationship between whole-facet albedo increase and temperature reduction is also observed for cool roofs (0.48 K / 0.23 K = 2.1). Adopting cool walls (roofs) leads to 0.054 K (0.060 K) canyon air temperature reduction per 0.10 whole-facet albedo increase in the COOL_WALL_HIGH (COOL_ROOF_HIGH) - CONTROL scenario. The ratios of daily average reductions induced by cool walls to those yielded by cool roofs are 83% and 90%, respectively, for whole-facet albedo increases of 0.40 and 0.80. Note that we also did three additional ensemble simulations for the scenario COOL_ROOF_WALL_HIGH where the albedos of walls and roofs are both raised to 0.90 to test the linearity of adopting cool walls and roofs simultaneously or separately. As shown in Table A5 in the Supporting Information, the reduction in canyon air temperature in COOL_ROOF_WALL_HIGH is approximately the sum of the reductions in COOL_WALL_HIGH and COOL_ROOF_HIGH relative to CONTROL. This suggests that the effects of adopting cool walls and roofs are additive.

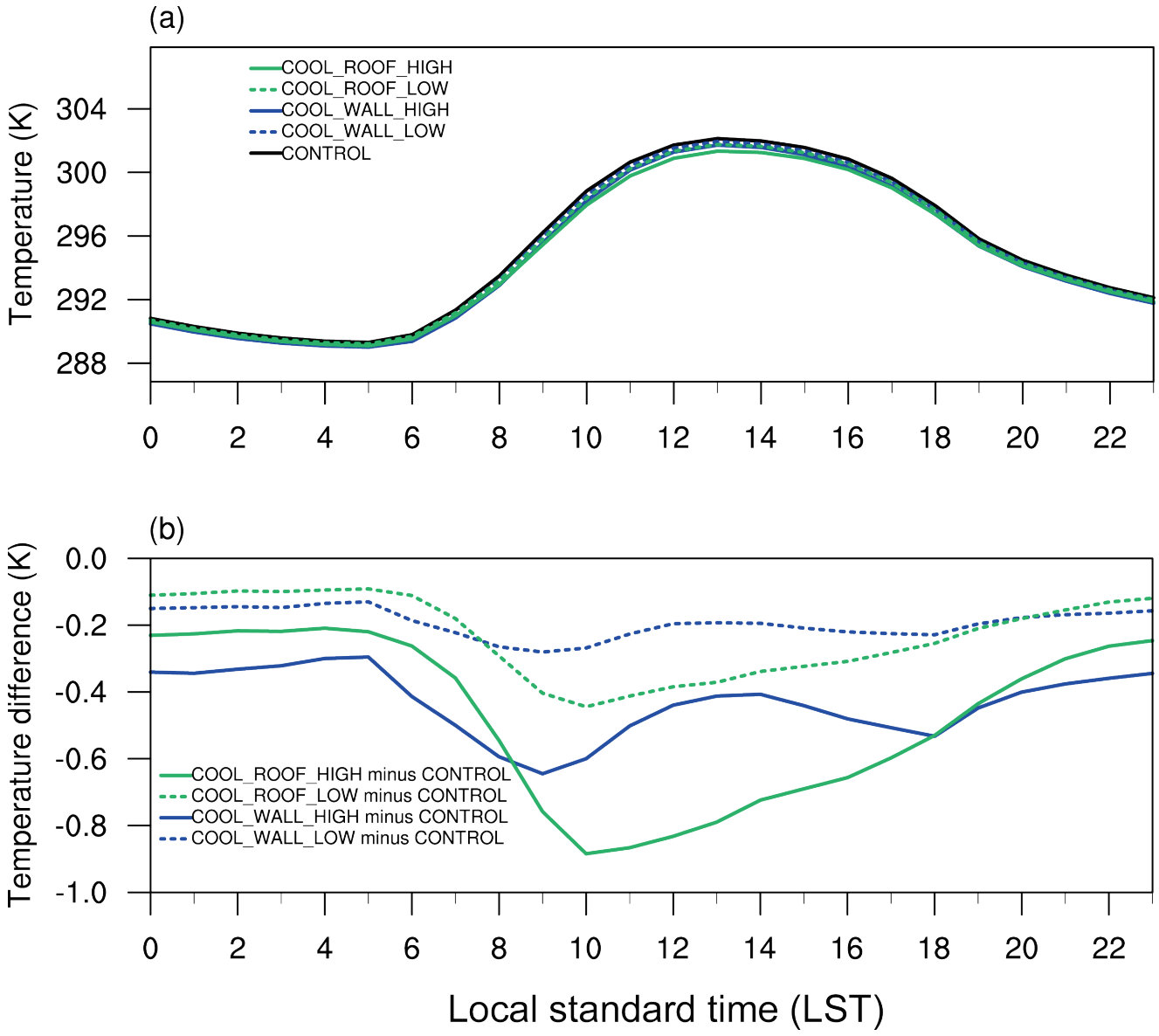

Figure 4. The diurnal cycle of (a) spatially averaged canyon air temperature (K) for CONTROL, COOL_WALL_LOW, COOL_WALL_HIGH, COOL_ROOF_LOW, and COOL_ROOF_HIGH; and (b) difference in canyon air temperatures for COOL_WALL_LOW – CONTROL, COOL_WALL_HIGH – CONTROL, COOL_ROOF_LOW – CONTROL, and COOL_ROOF_HIGH – CONTROL. Values represent spatial averages in Los Angeles County (i.e., shown in Figure 1b) for urban grid cells from 00:00 LST on July 3 to 00:00 LST on July 12.

3.4 Spatial variation of canyon air temperature

Figure 5 shows spatial variation in canyon air temperatures for the control, cool wall, and cool roof simulations at 14:00 LST and 20:00 LST. In CONTROL, desert regions and the eastern portion of the Los Angeles basin are hotter than the coastal regions, as expected. Employing cool walls and cool roofs reduces temperatures in the urban portions of the domain. Air

temperature decreases in inland urban areas are larger than those in coastal area. This is likely because the effects of cool walls and roofs accumulate as winds (which in Los Angeles are primarily due to sea breeze) advect air downstream from west to east. Cool walls lead to similar canyon air temperature reductions at 14:00 LST and 20:00 LST, while cool roofs cause larger temperature reductions at 14:00 LST than at 20:00 LST. Adopting cool walls shows a greater cooling effect than cool roofs with the same albedo rise relative to CONTROL at 20:00 LST, but a lesser cooling effect at 14:00 LST (Figure 5 and Table 3).

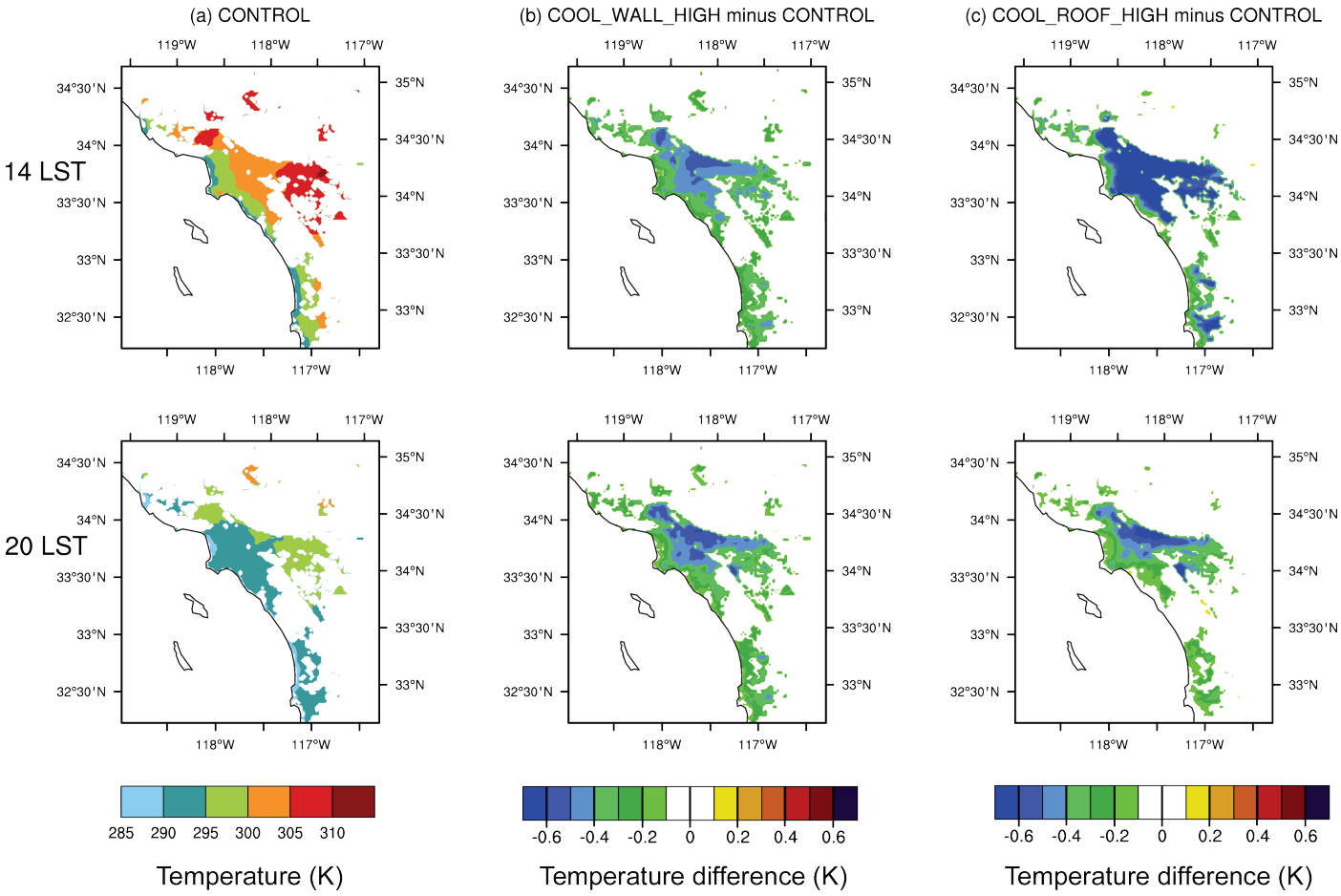

Figure 5. Simulated canyon air temperature (K) at 14:00 LST (top) and 20:00 LST (bottom) for (a) CONTROL, as well as the temperature differences for (b) COOL_WALL_HIGH – CONTROL, and (c) COOL_ROOF_HIGH – CONTROL. Values are temporally averaged over the period of 00:00 LST on July 3 to 00:00 LST on July 12.

3.5 Estimating whole-facet albedo increases from cool surface campaigns in Los Angeles

Assume that single-family homes and fast-food restaurants have high-slope roofs, and that all other buildings have low-slope roofs. From Table A4, there is 18.8M m² of low-slope roof area

and 22.7M m² of high-slope roof area in the City of Los Angeles. If a cool roof campaign in the City of Los Angeles modifies all gross roof area, raising the albedo of low-slope roofs by 0.40 (to aged albedo 0.60 from aged albedo 0.20) and the albedo of high-slope roofs by 0.15 (to aged albedo 0.25 from aged albedo 0.10), area weighting yields a city-mean whole-roof albedo rise of 0.26.

The citywide ratio of net wall area to gross wall area is 83% (Table A4). Levinson et al. (2018) found that 12 to 18 months of natural exposure lowers by only a few percentage points the albedo of a light-colored wall with initial albedo 0.60. If a cool wall campaign in LA excludes windows and doors, raising the albedo of the net wall areas by 0.33 (to aged albedo 0.58 from aged albedo 0.25), the city-mean rise in whole-wall albedo will be 83% × 0.33 = 0.27. Thus, the whole-wall albedo rise in the cool-wall campaign will be essentially equal to the whole-roof albedo rise in the cool-roof campaign.

4 Conclusions

Using the WRF model, we conduct simulations for July 2012 for three scenarios (CONTROL, COOL_WALL_LOW, and COOL_WALL_HIGH) to assess the influence of employing cool walls on albedo and climate. Three ensemble members per scenario are simulated to reduce the influence of model internal variability on simulated temperature changes. Whole-wall albedo increases for COOL_WALL_LOW and COOL_WALL_HIGH relative to CONTROL are 0.40 and 0.80, respectively. Urban grid cell albedo increases induced by cool walls peak in the early morning and late afternoon when the ratio of solar radiation onto vertical walls versus horizontal surfaces is at a maximum. On the other hand, downward solar radiation reaches its maximum at noon. Thus, the increase in reflected solar radiation (grid cell albedo increase multiplied by baseline downward solar radiation) induced by cool walls reaches its maximum at 10:00 and 15:00 LST. Daily cumulative increase in reflected solar radiation for COOL_WALL_HIGH relative to CONTROL is 783 kJ m^{-2}, or 43% of that for COOL_ROOF_HIGH (1,840 kJ m^{-2}). Factors that make the upflux increase resulting from raising whole-wall albedo differ from that caused by raising whole-roof albedo in the UCM include (a) the ratio of gross wall area to roof area (1.97); (b) the ratio of vertical (wall) to horizontal (roof) solar irradiance (power per unit area; ratio 0.38 over the analysis period); and (c) our assumption that all sunlight reflected by roofs escapes the urban canopy, while only 50 - 59% of that reflected by walls does so, because some is absorbed by the ground or opposing walls (Task Report Appendix B).

Increasing whole-wall albedo by 0.80 is simulated to reduce the spatial mean canyon air temperature in Los Angeles County by 0.43 K (daily average), with the peak reduction (0.64 K) occurring at 09:00 LST and a secondary local peak (0.53 K) at 18:00 LST. Temperature reduction peaks at 09:00 LST and 18:00 LST because of (a) high values of increased reflected solar radiation from the canopy and irradiance on vertical wall surfaces; and (b) low atmospheric mixing heights, which cause changes in surface albedo to have larger air temperature effects relative to when the planetary boundary layer is deeper. Average temperature reductions at

14:00 LST and 20:00 LST are 0.41 K and 0.40 K, respectively. Comparing temperature reductions for COOL_WALL_HIGH – CONTROL versus COOL_WALL_LOW – CONTROL show that the simulated air temperature reductions are nearly linearly related to cool wall albedo increase.

In this study, we also simulate the climate effects of employing cool roofs to systematically compare cool roofs to cool walls within a consistent modeling framework. In contrast to cool walls, cool roofs lead to a constant urban grid cell albedo rise throughout the day. During most times of day (besides early morning and late afternoon when solar zenith angle is high), the grid cell albedo and reflected solar radiation increases from implementing cool roofs are higher than cool walls, even for the same whole-facet albedo increases. The daily average canyon air temperature reduction induced by increasing whole-roof albedo by 0.80 is 0.48 K, slightly higher than that induced by cool walls (0.43 K) for equal increase in whole-wall albedo. Temperature reductions after implementing cool roofs at 14:00 and 22:00 LST are 0.72 K and 0.36 K, respectively. The peak temperature reduction from cool roofs (0.88 K) occurs at 10:00 LST due to the high solar irradiance and a relatively shallow planetary boundary layer.

Widespread adoption of cool walls (roofs) in Los Angeles County can reduce summertime daily average canyon air temperature by 0.048–0.054 K (0.058–0.060 K) per 0.10 increase in whole-wall (whole-roof) albedo. For equal increase in whole-facet albedo, the ratio of cool wall daily average canyon air temperature reduction induced by cool walls to that yielded by cool roofs is 83–90%. The temperature reductions induced by cool walls are larger at night and smaller during the day compared to cool roofs with the same whole-facet albedo increases. On the other hand, per 1 J m^{-2} increase in daily upflux, the daily-average canyon air temperature reduction induced by cool walls (0.55 μK) is twice that induced by cool roofs (0.26 μK).

Cool-wall air temperature reductions and solar upflux increases reported in this study should be multiplied by 0.83, the ratio of net wall area to gross wall area in the City of Los Angeles, if the albedos of windows and doors are unchanged in a cool-wall campaign. Finally, we estimate that in the City of Los Angeles, the whole-wall albedo increase from a cool-wall campaign that excludes windows and doors is essentially equal to the whole-roof albedo increase from a cool-roof campaign that modifies the entire roof.

5 Acknowledgements

Computation for the work described in this paper was supported by the University of Southern California's Center for High-Performance Computing (hpc.usc.edu). We thank Pablo Rosado for providing calculations on solar irradiance incident to surfaces with different orientations. We also thank Gert-Jan Steeneveld, Pouya Vahmani, Dan Li, Ravan Ahmadov, Stu McKeen, Trevor Krasowsky, Mo Chen, Mohammad Taleghani, Wei Tao, Joachim Fallmann, Haley Gilbert, and Junfeng Liu for their helpful suggestions.

References

Berdahl P, Akbari H, Levinson R, Miller WA. 2008. Weathering of roofing materials—An overview. Construction and Building Materials 22(4), 423-433. https://doi.org/10.1016/j.conbuildmat.2006.10.015

Bonan, G. B.: Ecological Climatology: Concepts and Applications, 2nd Edition., 2010.

Chen, F. and Dudhia, J.: Coupling an Advanced Land Surface–Hydrology Model with the Penn State–NCAR MM5 Modeling System. Part II: Preliminary Model Validation, Mon. Weather Rev., 129(4), 587–604, https://doi.org/10.1175/1520-0493(2001)129<0587:CAALSH>2.0.CO;2, 2001.

Chen, F., Kusaka, H., Bornstein, R., Ching, J., Grimmond, C. S. B., Grossman-Clarke, S., Loridan, T., Manning, K. W., Martilli, A., Miao, S., Sailor, D., Salamanca, F. P., Taha, H., Tewari, M., Wang, X., Wyszogrodzki, A. A. and Zhang, C.: The integrated WRF/urban modelling system: Development, evaluation, and applications to urban environmental problems, *Int. J. Climatol.*, 31(2), 273–288, https://doi.org/10.1002/joc.2158, 2011.

Ching, J., Brown, M., Burian, S., Chen, F., Cionco, R., Hanna, A., Hultgren, T., McPherson, T., Sailor, D., Taha. H., and Williams, D.: National urban database and access portal tool, *Bull. Am. Meteorol.* Soc., 90(8), 1157–1168, https://doi.org/10.1175/2009BAMS2675.1, 2009.

Chou, M-D., and M. J. Suarez, 1994: An efficient thermal infrared radiation parameterization for use in general circulation models. NASA Tech. Memo. 104606, http://citeseerx.ist.psu.edu/viewdoc/download?doi=10.1.1.26.4850&rep=rep1&type=pdf.

Duffie JA, Beckman WA. 2006. *Solar Engineering of Thermal Processes*, 3rd ed. Wiley.

Fan, H. and Sailor, D. J.: Modeling the impacts of anthropogenic heating on the urban climate of Philadelphia: A comparison of implementations in two PBL schemes, *Atmos. Environ.*, 39(1), 73–84, https://doi.org/10.1016/j.atmosenv.2004.09.031, 2005.

Fry, J. A., Xian, G., Jin, S., Dewitz, J. A., Homer, C. G., Yang, L., Barnes, C. A., Herold, N. D. and Wickham, J. D.: Completion of the 2006 National Land Cover Database for the conterminous United States, *Photogramm. Eng. Remote Sensing*, 77, 858–566, 2011.

Georgescu, M., Morefield, P. E., Bierwagen, B. G. and Weaver, C. P.: Urban adaptation can roll back warming of emerging megapolitan regions, *Proc. Natl. Acad. Sci.*, 111(8), 2909–2914, https://doi.org/10.1073/pnas.1322280111, 2014.

Hong, S.-Y., Noh, Y. and Dudhia, J.: A New Vertical Diffusion Package with an Explicit Treatment of Entrainment Processes, *Mon. Weather Rev.*, 134(9), 2318–2341, https://doi.org/10.1175/MWR3199.1, 2006.

Kain, J. S.: The Kain–Fritsch Convective Parameterization: An Update, *J. Appl. Meteorol.*, 43(1), 170–181, https://doi.org/10.1175/1520-0450(2004)043<0170:TKCPAU>2.0.CO;2, 2004.

Kolokotroni, M., Giannitsaris, I. and Watkins, R.: The effect of the London urban heat island on building summer cooling demand and night ventilation strategies, *Sol. Energy*, 80(4), 383–392, https://doi.org/10.1016/j.solener.2005.03.010, 2006.

Kusaka, H., Kondo, H., Kikegawa, Y. and Kimura, F.: A simple single-layer urban canopy model for atmospheric models: Comparison with multi-layer and slab models, *Boundary-Layer Meteorol.*, 101(3), 329–358, https://doi.org/10.1023/A:1019207923078, 2001.

LARIAC: LA County Street & Address File, [online] Available from: https://egis3.lacounty.gov/dataportal/2014/06/16/2011-la-county-street-centerline-street-address-file (Accessed 3 August 2017), 2014.

LARIAC: Countywide Building Outlines, [online] Available from: https://egis3.lacounty.gov/dataportal/lariac/ (Accessed 11 July 2017), 2016.

Levinson R, et al. 2018. Solar-reflective “cool” walls: Benefits, technologies, and implementation. California Energy Commission. Publication Number: CEC-XXX-201X-XXX. Draft online at http://goo.gl/kPqjeu .

Levinson R, Berdahl P, Akbari H, Miller W, Joedicke I, Reilly J, Suzuki Y, Vondran M. 2007. Methods of creating solar-reflective nonwhite surfaces and their application to residential roofing materials. *Solar Energy Materials & Solar Cells* 91, 304-314. https://doi.org/10.1016/j.solmat.2006.06.062

Li, D. and Bou-Zeid, E.: Quality and sensitivity of high-resolution numerical simulation of urban heat islands, *Environ. Res. Lett.*, 9(5), https://doi.org/10.1088/1748-9326/9/5/055001, 2014.

Li, D., Bou-Zeid, E. and Oppenheimer, M.: The effectiveness of cool and green roofs as urban heat island mitigation strategies, *Environ. Res. Lett.*, 9(5), https://doi.org/10.1088/1748-9326/9/5/055002, 2014.

Lin, Y.-L., Farley, R. D. and Orville, H. D.: Bulk Parameterization of the Snow Field in a Cloud Model, *J. Clim. Appl. Meteorol.*, 22(6), 1065–1092, https://doi.org/10.1175/1520-0450(1983)022<1065:BPOTSF>2.0.CO;2, 1983.

Mesinger, F., DiMego, G., Kalnay, E., Mitchell, K., Shafran, P. C., Ebisuzaki, W., Jović, D., Woollen, J., Rogers, E., Berbery, E. H., Ek, M. B., Fan, Y., Grumbine, R., Higgins, W., Li, H., Lin, Y., Manikin, G., Parrish, D. and Shi, W.: North American regional reanalysis, *Bull. Am. Meteorol. Soc.*, 87(3), 343–360, https://doi.org/10.1175/BAMS-87-3-343, 2006.

Millstein, D. and Menon, S.: Regional climate consequences of large-scale cool roof and photovoltaic array deployment, *Environ. Res. Lett.*, 6(3), https://doi.org/10.1088/1748-9326/6/3/034001, 2011.

Mlawer, E. J., Taubman, S. J., Brown, P. D., Iacono, M. J. and Clough, S. A.: Radiative transfer for inhomogeneous atmospheres: RRTM, a validated correlated-k model for the longwave, J. *Geophys. Res. Atmos.*, 102(D14), 16663–16682, https://doi.org/10.1029/97JD00237, 1997.

Mohegh, A., Rosado, P., Jin, L., Millstein, D., Levinson, R. and Ban-Weiss, G.: Modeling the climate impacts of deploying solar reflective cool pavements in California cities, *J. Geophys. Res.*, 122(13), 6798–6817, https://doi.org/10.1002/2017JD026845, 2017.

NREL. 2017. PVWatts Calculator Model. National Renewable Energy Laboratory (NREL). http://pvwatts.nrel.gov .

Oke, T. R., Johnson, G. T., Steyn, D. G. and Watson, I. D.: Simulation of surface urban heat islands under "ideal" conditions at night part 2: Diagnosis of causation, *Boundary-Layer Meteorol.*, 56(4), 339–358, https://doi.org/10.1007/BF00119211, 1991.

Palecki, M. A., Changnon, S. A. and Kunkel, K. E.: The nature and impacts of the July 1999 heat wave in the midwestern United States: Learning from the lessons of 1995, *Bull. Am. Meteorol.* Soc., 82(7), 1353–1367, https://doi.org/10.1175/1520-0477(2001)082<1353:TNAIOT>2.3.CO;2, 2001.

Rosado, P. J.: Evaluating Cool Impervious Surfaces: Application to an Energy-Efficient Residential Roof and to City Pavements, University of California, Berkeley. [online] Available from: https://escholarship.org/uc/item/6bf80485.

Rosenfeld, A. H., Akbari, H., Romm, J. J. and Pomerantz, M.: Cool communities: Strategies for heat island mitigation and smog reduction, *Energy Build.*, 28(1), 51–62, https://doi.org/10.1016/S0378-7788(97)00063-7, 1998.

Santamouris, M.: Cooling the cities - A review of reflective and green roof mitigation technologies to fight heat island and improve comfort in urban environments, *Sol. Energy*, 103, 682–703, https://doi.org/10.1016/j.solener.2012.07.003, 2014.

Skamarock, W. C., Klemp, J. B., Dudhi, J., Gill, D. O., Barker, D. M., Duda, M. G., Huang, X.-Y., Wang, W. and Powers, J. G.: A Description of the Advanced Research WRF Version 3, NCAR Tech. Note, (June), 113, https://doi.org/10.5065/D6DZ069T, 2008.

Sleiman M, Ban-Weiss G, Gilbert HE, Francois D, Berdahl P, Kirchstetter TW, Destaillats H, Levinson R. 2011. Soiling of building envelope surfaces and its effect on solar reflectance—Part I: Analysis of roofing product databases. Solar Energy Materials & Solar Cells 95, 3385-3399. https://doi.org/10.1016/j.solmat.2013.11.028

Synnefa, A., Dandou, A., Santamouris, M., Tombrou, M. and Soulakellis, N.: On the use of cool materials as a heat island mitigation strategy, *J. Appl. Meteorol. Climatol.*, 47(11), 2846–2856, https://doi.org/10.1175/2008JAMC1830.1, 2008.

Taha, H.: Urban climates and heat islands: albedo, evapotranspiration, and anthropogenic heat, *Energy Build.*, 25(2), 99–103, https://doi.org/10.1016/S0378-7788(96)00999-1, 1997.

Taha, H.: Meso-urban meteorological and photochemical modeling of heat island mitigation, *Atmos. Environ.*, 42(38), 8795–8809, https://doi.org/10.1016/j.atmosenv.2008.06.036, 2008.

Theeuwes, N. E., Steeneveld, G. J., Ronda, R. J., Heusinkveld, B. G., van Hove, L. W. A. and Holtslag, A. A. M.: Seasonal dependence of the urban heat island on the street canyon aspect ratio, *Q. J. R. Meteorol. Soc.,* 140(684), 2197–2210, https://doi.org/10.1002/qj.2289, 2014.

Theeuwes, N. E., Steeneveld, G. J., Ronda, R. J., Rotach, M. W. and Holtslag, A. A. M.: Cool city mornings by urban heat, *Environ. Res. Lett.,* 10(11), https://doi.org/10.1088/1748-9326/10/11/114022, 2015.

Vahmani, P. and Ban-Weiss, G.: Climatic consequences of adopting drought-tolerant vegetation over Los Angeles as a response to California drought, *Geophys. Res. Lett.*, 43(15), 8240–8249, https://doi.org/10.1002/2016GL069658, 2016a.

Vahmani, P. and Ban-Weiss, G.: Impact of Remotely Sensed Albedo and Vegetation Fraction on Simulation of Urban Climate in WRF-UCM: A Case Study of the Urban Heat Island in Los Angeles, *J. Geophys. Res. Atmos.*, 121(4), 1511–1531, https://doi.org/10.1002/2015JD023718, 2016b.

Vahmani, P., Sun, F., Hall, A. and Ban-Weiss, G.: Investigating the climate impacts of urbanization and the potential for cool roofs to counter future climate change in Southern California, *Environ. Res. Lett.*, 11(12), https://doi.org/10.1088/1748-9326/11/12/124027, 2016.

Warner, T. T.: *Numerical Weather and Climate Prediction.*, Cambridge, 2011.

Wickham, J. D., Stehman, S. V., Gass, L., Dewitz, J., Fry, J. A. and Wade, T. G.: Accuracy assessment of NLCD 2006 land cover and impervious surface, *Remote Sens. Environ.*, 130, 294–304, https://doi.org/10.1016/j.rse.2012.12.001, 2013.

Task Report Appendix A

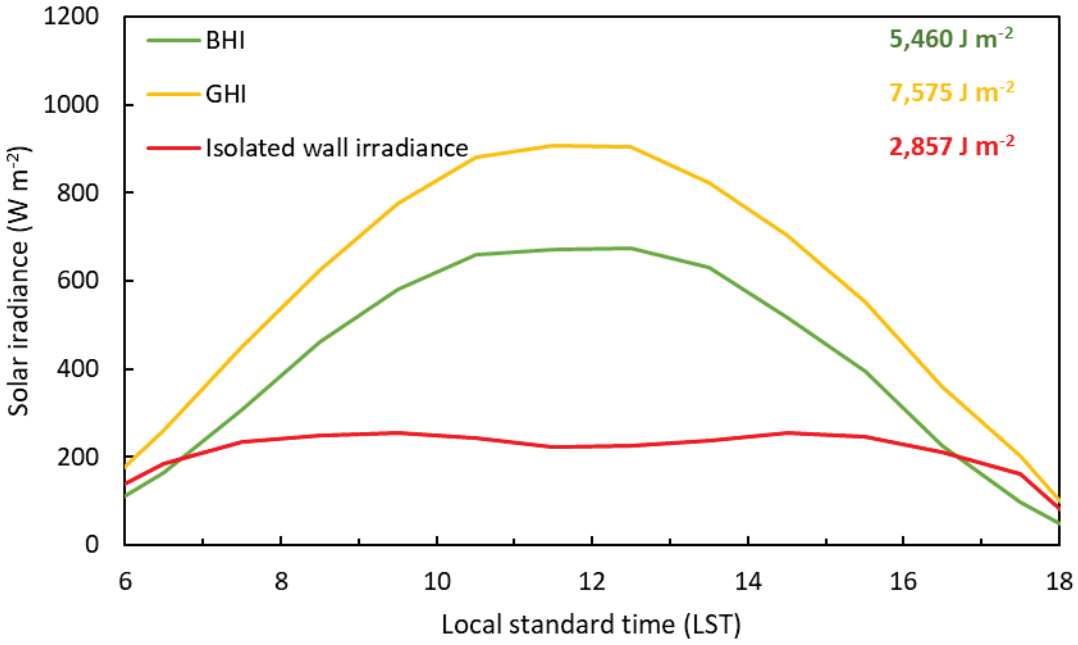

Figure A1. Diurnal cycles of beam horizontal irradiance (BHI), global horizontal irradiance (GHI), and isolated wall irradiance in Burbank, CA, averaged by hour of day in July. BHI and GHI are obtained from the typical meteorological year 3 (TMY3) file for station 722880 (Burbank-Glendale-Pasadena AP); isolated wall irradiance is the average of global tilt irradiances for north, east, south, and west walls without neighbors, computed with the standard isotropic sky model (Duffie and Beckman 2006) and assuming a ground albedo of 0.10. Daily beam horizontal irradiation (energy per unit area), global horizontal irradiation, and isolated wall irradiation are tabulated in the upper right corner.

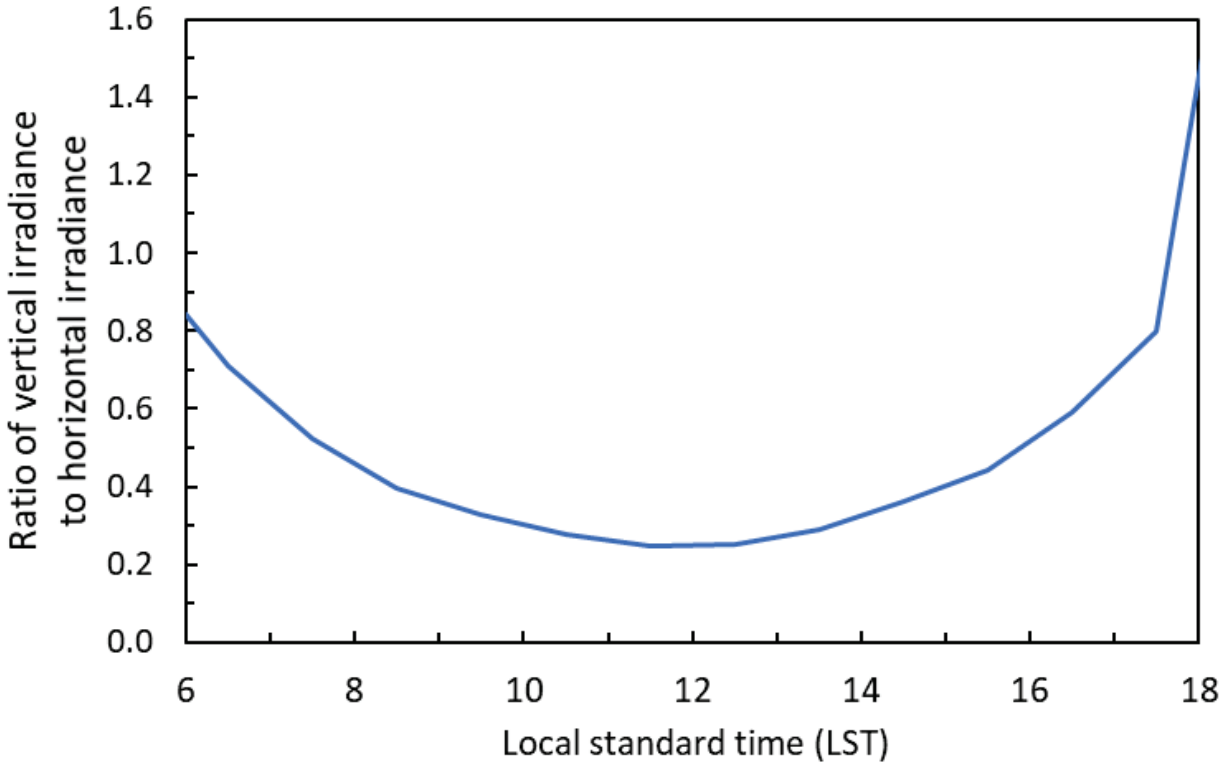

Figure A2. Diurnal cycle of the ratio between the isolated wall irradiance (vertical irradiance) and the global horizontal irradiance (GHI) shown in Figure A1.

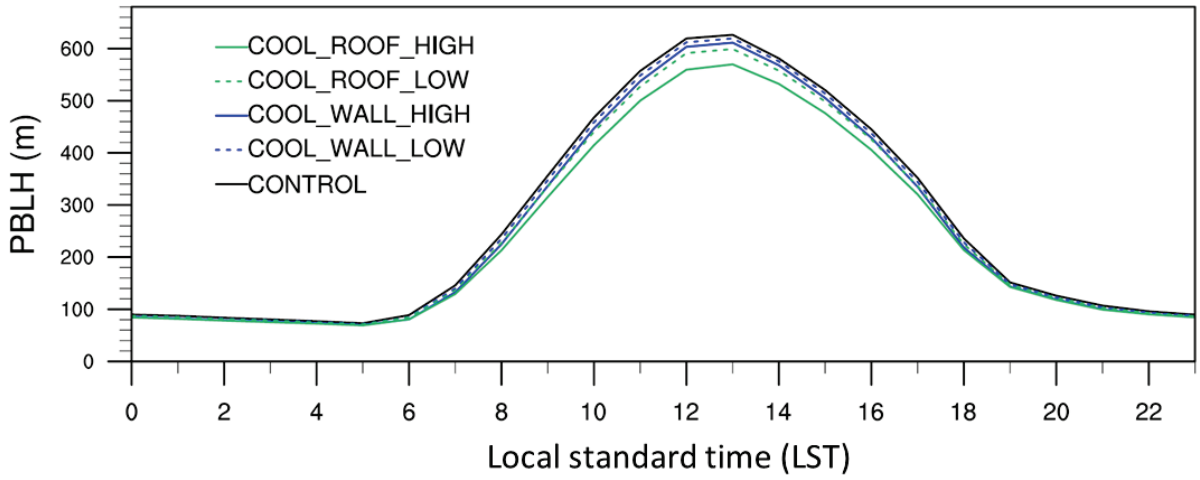

Figure A3. The diurnal cycle of spatially averaged planetary boundary layer height (PBLH) for CONTROL, COOL_WALL_LOW, COOL_WALL_HIGH, COOL_ROOF_LOW, and COOL_ROOF_HIGH. Values represent spatial averages in Los Angeles County (main article Figure1b) for urban grid cells from 00:00 LST on July 3 to 00:00 LST on July 12.

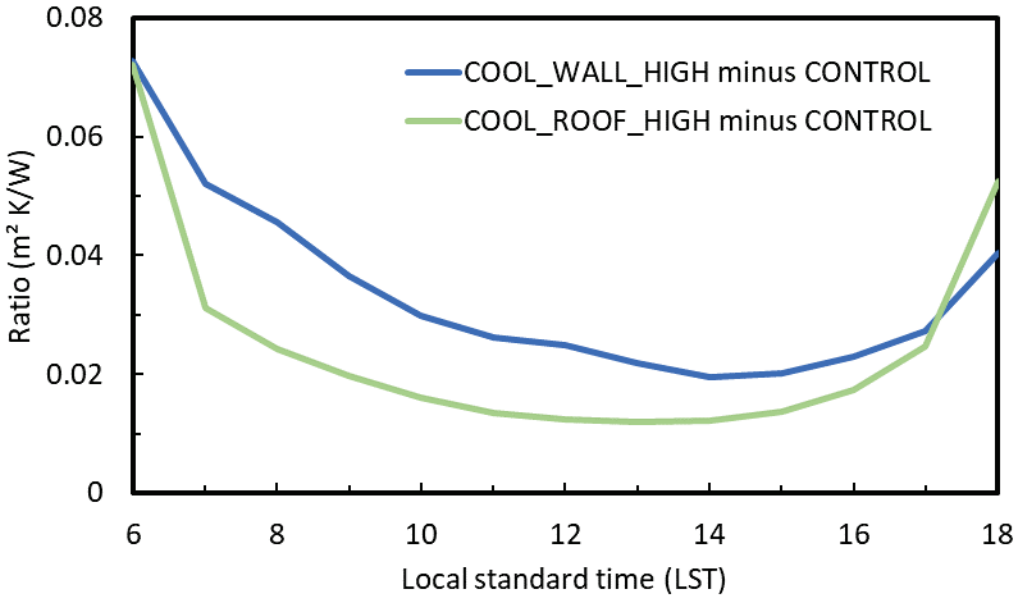

Figure A4. Increases (COOL_WALL_HIGH – CONTROL and COOL_ROOF_HIGH – CONTROL) in the ratio of canyon air temperature reduction (K) to increase in reflected solar radiation (W m^{-2}).

Table A1. Monthly and seasonal daily solar irradiation in Burbank, California (TMY3 station 722880), computed with PVWatts (NREL 2017).

		Solar Radiation [kWh/m²·day]						
		Horizontal (H)	North wall (N)	East wall (E)	South wall (S)	West wall (W)	Four-wall average (NESW)	Ratio of NESW to H
Month	January	**2.97**	**0.65**	**1.96**	**4.56**	**1.81**	**2.25**	**76%**
	February	**3.19**	**0.81**	**1.82**	**3.33**	**1.88**	**1.96**	**61%**
	March	**4.99**	**0.99**	**2.68**	**3.76**	**2.81**	**2.56**	**51%**
	April	**6.42**	**1.26**	**3.28**	**3.06**	**3.59**	**2.80**	**44%**
	May	**6.74**	**1.70**	**3.53**	**2.30**	**3.62**	**2.79**	**41%**
	June	**7.79**	**1.90**	**3.70**	**2.17**	**4.06**	**2.96**	**38%**
	July	**7.60**	**1.91**	**4.14**	**2.43**	**3.98**	**3.11**	**41%**
	August	**7.23**	**1.51**	**3.92**	**3.26**	**4.05**	**3.19**	**44%**
	September	**5.36**	**1.22**	**3.11**	**3.77**	**3.28**	**2.84**	**53%**
	October	**3.90**	**0.96**	**2.47**	**4.02**	**2.24**	**2.42**	**62%**
	November	**3.56**	**0.79**	**2.23**	**5.15**	**2.38**	**2.64**	**74%**
	December	**2.66**	**0.67**	**1.79**	**4.41**	**1.84**	**2.18**	**82%**
Season	Winter (DJF)	**2.94**	**0.71**	**1.86**	**4.10**	**1.84**	**2.13**	**72%**
	Spring (MAM)	**6.05**	**1.31**	**3.17**	**3.04**	**3.34**	**2.71**	**45%**
	Summer (JJA)	**7.54**	**1.77**	**3.92**	**2.62**	**4.03**	**3.09**	**41%**
	Fall (SON)	**4.27**	**0.99**	**2.60**	**4.31**	**2.63**	**2.63**	**62%**
Ratio	Winter / Summer	**39%**	**40%**	**47%**	**157%**	**46%**	**69%**	

Table A2. Same as Table A1, but for Riverside, California (TMY3 station 722880).

		Solar Radiation [kWh/m²·day]						
		Horizontal (H)	North wall (N)	East wall (E)	South wall (S)	West wall (W)	Four-wall average (NESW)	Ratio of NESW to H
Month	January	**3.09**	**0.75**	**1.87**	**4.62**	**2.06**	**2.33**	**75%**
	February	**3.51**	**0.92**	**2.14**	**3.93**	**2.21**	**2.30**	**66%**
	March	**4.87**	**1.07**	**2.42**	**3.69**	**2.96**	**2.54**	**52%**
	April	**6.17**	**1.39**	**3.46**	**3.15**	**3.38**	**2.84**	**46%**
	May	**6.91**	**1.77**	**3.36**	**2.45**	**3.89**	**2.87**	**41%**
	June	**7.92**	**2.02**	**3.76**	**2.26**	**4.24**	**3.07**	**39%**
	July	**7.61**	**1.98**	**4.14**	**2.46**	**4.04**	**3.16**	**41%**
	August	**7.12**	**1.59**	**3.96**	**3.24**	**3.93**	**3.18**	**45%**
	September	**4.93**	**1.22**	**2.90**	**3.42**	**2.95**	**2.62**	**53%**
	October	**3.83**	**0.99**	**2.28**	**3.84**	**2.27**	**2.34**	**61%**
	November	**3.55**	**0.82**	**2.20**	**5.06**	**2.34**	**2.60**	**73%**
	December	**2.94**	**0.73**	**2.02**	**4.95**	**1.98**	**2.42**	**82%**
Season	Winter (DJF)	**3.18**	**0.80**	**2.01**	**4.50**	**2.09**	**2.35**	**74%**
	Spring (MAM)	**5.98**	**1.41**	**3.08**	**3.10**	**3.41**	**2.75**	**46%**
	Summer (JJA)	**7.55**	**1.86**	**3.95**	**2.65**	**4.07**	**3.14**	**42%**
	Fall (SON)	**4.10**	**1.01**	**2.46**	**4.11**	**2.52**	**2.52**	**62%**
Ratio	Winter / Summer	**42%**	**43%**	**51%**	**169%**	**51%**	**75%**	

Table A3. Number of buildings included in LARIAC (2016) dataset for the three urban land use types and corresponding mean roof area and mean gross wall area.

Urban land use type	Number of buildings	Mean roof area (m^2)	Mean gross wall area (m^2)
Low-intensity residential	243,098	5,274	9,094
High-intensity residential	1,854,746	4,474	7,481
Commercial and industrial	111,187	8,726	13,094

Table A4. Conditioned floor area, roof area, net wall area, and gross wall area for DOE building prototypes reported by Levinson et al. (2018), and total floor areas in the City of Los Angeles attributed to each building category (Rosado 2016). Total roof, net wall, or gross wall area in the city by building category is calculated as total floor area times the ratio of prototype roof, net wall, or gross wall area to prototype conditioned floor area.

Building category	Prototype conditioned floor area (m^2)	Prototype roof area (m^2)	Prototype net wall area (m^2)	Prototype gross wall area (m^2)	Total floor area in city (m^2)	Total roof area in city (m^2)	Total net wall area in city (m^2)	Total gross wall area in city (m^2)	Ratio of total net wall area to total gross wall area in city
Single-family home	223	112	184	221	45,530,404	22,772,286	37,594,855	45,160,276	0.83
Apartment building	2,010	669	1,174	1,421	38,504,750	12,819,748	22,492,230	27,223,469	0.83
Small office	511	511	222	282	NA	N/A	NA	NA	NA
Medium office	4,980	1,661	1,325	1,978	3,727,395	1,243,011	991,592	1,480,225	0.67
Large office	46,300	3,563	6,953	11,590	2,261,120	174,009	339,577	565,990	0.60
Large hotel	11,400	1,979	2,812	4,026	1,223,986	212,452	301,911	432,262	0.70
Retail stand-alone	2,290	2,264	1,093	1,177	381,447	377,159	182,075	196,057	0.93
Retail strip mall	2,090	2,072	1,060	1,184	3,589,683	3,559,591	1,820,347	2,033,822	0.90
Fast-food restaurant	232	232	160	186	612	613	422	490	0.86
Sit-down restaurant	511	511	229	276	461,927	462,063	206,593	249,242	0.83
LA sum or ratio					95,681,324	41,620,933	63,929,602	77,341,834	0.83

Table A5. Urban grid cell albedo, upflux (reflected solar radiation) [a], and canyon air temperature at different times of day in Los Angeles County (shown in Figure 1b), including absolute values for CONTROL, changes relative to CONTROL for the five perturbation scenarios, and the sum of COOL_WALL_HIGH minus CONTROL and COOL_ROOF_HIGH minus CONTROL. [b]

Scenario	Albedo at 06:00 LST	Albedo at 12:00 LST	Daily average solar upflux (W m^{-2})	Daily (24-hour) average canyon air temperature (K)	Canyon air temperature (K) at 14:00 LST	Canyon air temperature (K) at 20:00 LST
CONTROL	0.143	0.148	50.2	295.2	302	294.5
COOL_WALL_LOW minus CONTROL	0.045	0.008	4.3	-0.19	-0.19	-0.18
COOL_WALL_HIGH minus CONTROL	0.097	0.017	9.1	-0.43	-0.41	-0.4
COOL_ROOF_LOW minus CONTROL	0.033	0.033	10.7	-0.23	-0.34	-0.18
COOL_ROOF_HIGH minus CONTROL	0.065	0.065	21.3	-0.48	-0.72	-0.36
COOL_ROOF_WALL_HIGH minus CONTROL	0.162	0.083	30.1	-0.95	-1.17	-0.78
COOL_WALL_HIGH minus CONTROL + COOL_ROOF_HIGH minus CONTROL	0.162	0.082	30.4	-0.91	-1.13	-0.76

[a] Daily average solar upflux (W m^{-2}) multiplied by 86,400 seconds (24 hours) is equal to daily cumulative solar upflux (J m^{-2}).

[b] All values are averages for July 3 to 12.

Task Report Appendix B

We define variables as follows.

$F_{W\to S}$ is view factor from wall to sky.

$F_{G\to S}$ is view factor from ground to sky.

$F_{W\to W}$ is view factor from wall to wall.

$F_{W\to G}$ is view factor from wall to ground.

$\propto_G$ is ground albedo ($\propto_G = 0.10$).

$\propto_W$ is wall albedo.

$$\propto_W = \begin{cases} 0.10 & \text{(CONTROL)} \\ 0.50 & \text{(COOL\_WALL\_LOW)} \\ 0.90 & \text{(COOL\_WALL\_HIGH)} \end{cases}$$

f is the fraction of solar radiation reflected by walls that escapes the canopy.

Table 1 in main article shows urban morphology configuration for grid cells where NLCD land use types are not used. View factors are calculated based on the morphology for each land use type.

The WRF model approximates f by

$$f_{WRF} = F_{W\to S} + F_{W\to W} \times \propto_W + F_{W\to G} \times \propto_G \quad \text{(B-1)}$$

Table B1 reports f_{WRF} in the control scenario and the two cool wall scenarios.

f_{WRF} overestimates f because its calculation assumes that all wall-reflected light subsequently reflected by the wall or ground will escape the canopy. That is, it neglects absorption of this light by wall or ground.

We develop a lower bound estimate for f, denoted f_L (Table B2), that assumes that of the wall-reflected light subsequently reflected by wall or ground, only that portion immediately reflected toward the sky will escape the canopy:

$$f_L = F_{W\to S} + F_{W\to W} \times \propto_W \times F_{W\to S} + F_{W\to G} \times \propto_G \times F_{G\to S} \quad \text{(B-2)}$$

Thus f lies between f_L and f_{WRF}. For example, the true fraction of wall-reflected light that escapes the canopy in the low-intensity residential region is in the range 0.48 – 0.50 for CONTROL, 0.50 – 0.54 for COOL_WALL_LOW, and 0.54 – 0.59 for COOL_WALL_HIGH. The WRF model assumes $f = f_{WRF}$ (i.e., 0.50, 0.54, or 0.59) in these three scenarios.

If needed, one can either add 3rd (and 4th) reflections in the model code or use a wall albedo that corrects for the lack of 3rd (and 4th) reflections.

Table B1. View factors and fraction f_{WRF} of wall-reflected light that escapes the canopy in the WRF urban canopy model, shown by urban land use type for the control scenario and the two cool wall scenarios.

Urban land use type	View factor from wall to ground	View factor from wall to sky	View factor from wall to wall	Fraction of solar radiation reflected by walls that escapes canopy (CONTROL)	Fraction of solar radiation reflected by walls that escapes canopy (COOL_WALL_LOW)	Fraction of solar radiation reflected by walls that escapes canopy (COOL_WALL_HIGH)
Low-intensity residential	**0.45**	**0.45**	**0.11**	**0.50**	**0.54**	**0.59**
High-intensity residential	**0.45**	**0.45**	**0.11**	**0.50**	**0.54**	**0.59**
Commercial/ industrial	**0.44**	**0.44**	**0.12**	**0.50**	**0.54**	**0.59**

Table B2. Same as Table B1, but reporting lower-bound f_{L} to the fraction of wall-reflected light that escapes the canopy.

Urban land use type	View factor from wall to ground	View factor from wall to sky	View factor from wall to wall	Fraction of solar radiation reflected by walls that escapes canopy (CONTROL)	Fraction of solar radiation reflected by walls that escapes canopy (COOL_WALL_LOW)	Fraction of solar radiation reflected by walls that escapes canopy (COOL_WALL_HIGH)
Low-intensity residential	**0.45**	**0.45**	**0.11**	**0.48**	**0.50**	**0.54**
High-intensity residential	**0.45**	**0.45**	**0.11**	**0.48**	**0.50**	**0.54**
Commercial/ industrial	**0.44**	**0.44**	**0.12**	**0.47**	**0.51**	**0.55**

Task Report Appendix C

Figure C1 shows that the relationship between reduction in canyon air temperature (K) and the ratio of increase in upflux (W m^{-2}) to PBLH (m) is approximately linear for cool roofs, but not for cool walls. However, if we exclude two outliers at 06:00 and 07:00 LST (Figure C2), reduction in canyon air temperature per unit increase in the ratio of upflux (W m^{-2}) to PBLH (m) shows improved linearity (i.e., a higher coefficient of determination). (Note that at 06:00 and 07:00 LST, the surface has just begun to warm from solar radiation. In contrast, at later hours of day, the cooling induced by cool walls is influenced not only by instantaneous increase in upflux, but also by the accumulated reduction in absorbed solar heat gain (induced by increase in upflux) during previous hours of day.)

Figures C1 and C2 suggest that the PBLH and increase in upflux both contribute to the diurnal cycle of canyon air temperature reductions from adopting cool walls and roofs. PBLH is negatively correlated with the temperature reductions, while increase in upflux is positively correlated with the temperature reductions.

As described in the main article, we should also note that there are three competing processes contributing to the diurnal cycle of temperature reduction, and the system is more complicated than a linear model.

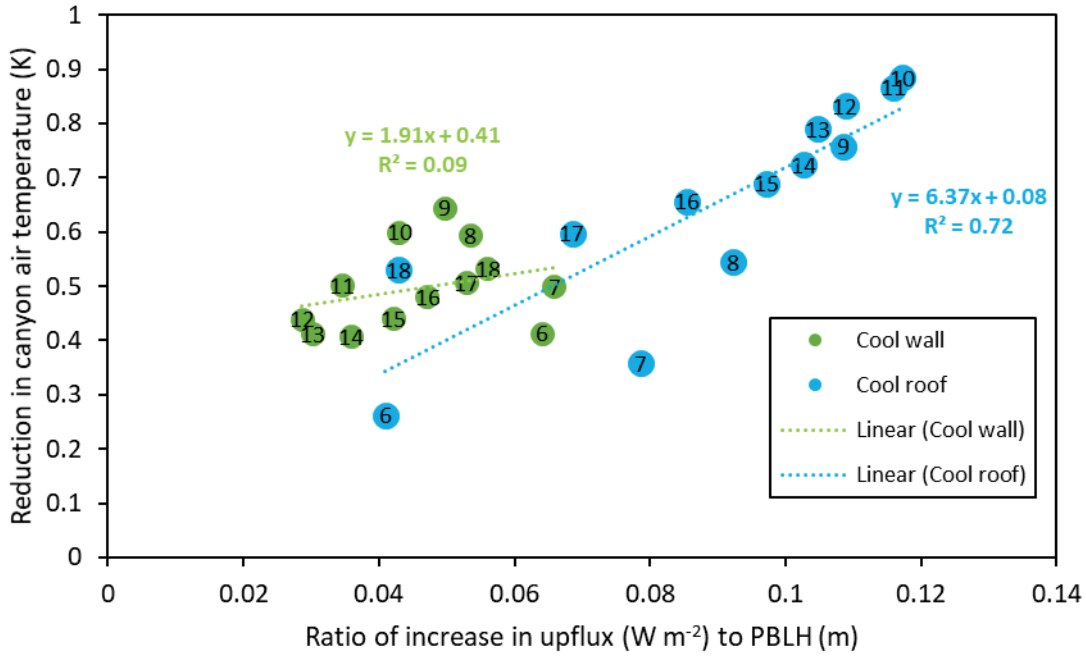

Figure C1. Scatter plot showing reductions in canyon air temperature (K) induced by cool walls (green) and cool roofs (blue) versus the ratio of increase in upflux (W m^{-2}) to PBLH height (m) in CONTROL. Numbers on dots label time of day (e.g., 6 = 06:00 LST). Least-squares linear regressions and corresponding coefficients of determination (R^2) for cool walls and roofs are also shown.

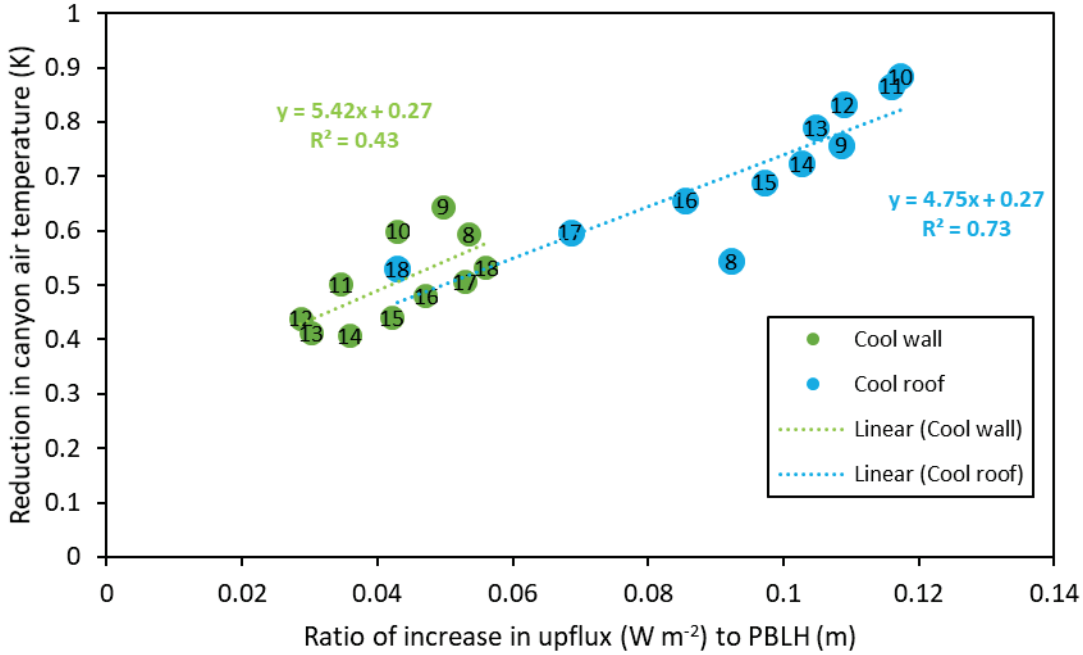

Figure C2. Same as Figure C1, but with data points corresponding to 06:00 and 07:00 LST removed.